atmosphere

MDPI

Article

Effect of Blue–Green Infrastructure in Mitigating Microenvironmental Heat Islands: Field- and Simulation-Based Insights

Tingzhen Ming [1,2], Yiwei Hu [1], Tianhao Shi [1,*], Yuewen Li [3], Shanjiang Hu [1], Di Yang [1], Bing Lv [1], Chong Peng [3] and Yanhua Chen [4]

[1] School of Civil Engineering and Architecture, Wuhan University of Technology, Wuhan 430070, China
[2] Sanya Science and Education Innovation Park, Wuhan University of Technology, Sanya 572004, China
[3] School of Architecture and Urban Planning, Huazhong University of Science and Technology, Wuhan 430074, China
[4] CITIC General Institute of Architectural Design and Research Co., Ltd., Wuhan 430014, China
* Correspondence: thshi@whut.edu.cn

Abstract: Urban heat island (UHI) effects, intensified by urbanization and environmental changes, are critical challenges to urban thermal comfort and sustainability. This study investigates the combined role of water bodies and vegetation in mitigating microclimatic heat island effects within a campus area, focusing on their cooling impacts and interactions. Using field measurements and numerical simulations, the research evaluates the cooling effects and wind flow modifications induced by greenery and water bodies in the surrounding environment. The findings demonstrate that both vegetation and water bodies provide a significant cooling effect, reducing temperatures by 0–6 K in downstream regions, with the impact being more pronounced closer to the blue–green spaces. Furthermore, the combined application of water bodies and vegetation offers enhanced cooling effects; however, their influence on the thermal environment exhibits a nonlinear relationship. These results underscore the importance of strategic blue–green infrastructure planning in mitigating UHI effects and optimizing urban thermal environments.

Keywords: blue–green infrastructure; microenvironment; urban heat island; computational fluid dynamics

Academic Editor: Teodoro Georgiadis

Received: 31 December 2024
Revised: 17 January 2025
Accepted: 24 January 2025
Published: 27 January 2025

Citation: Ming, T.; Hu, Y.; Shi, T.; Li, Y.; Hu, S.; Yang, D.; Lv, B.; Peng, C.; Chen, Y. Effect of Blue–Green Infrastructure in Mitigating Microenvironmental Heat Islands: Field- and Simulation-Based Insights. *Atmosphere* **2025**, *16*, 134. https://doi.org/10.3390/atmos16020134

1. Introduction

Urbanization is one of the most prominent trends of the 21st century, particularly in rapidly developing countries like China. As cities grow, the concentration of human activity and energy consumption increases, leading to significant amounts of waste heat being released into the atmosphere. This phenomenon has exacerbated the urban heat island (UHI) effect, where urban areas experience significantly higher temperatures than their rural counterparts. As a result, UHI has emerged as a critical challenge to urban sustainability, impacting both thermal comfort and public health. Moreover, with the growing frequency of extreme heat events worldwide, mitigating UHI has become crucial to achieving climate resilience in cities.

In response to these challenges, researchers have explored various strategies to mitigate the UHI effect. In earlier years, research was carried out on the impact of regional land use patterns on the heat island, and it was found that the air temperature of construction land is higher than that of residential and agricultural land [1]. Subsequently, many researchers

have attempted to mitigate the urban heat island by altering the properties of the underlying surface. For example, high-reflectivity coatings, such as cool roof materials and cool-color roof materials, have been applied in urban areas [2–4]. Among the most commonly discussed measures are green infrastructure (such as vegetation and urban forests) and blue infrastructure (including rivers, ponds, and lakes). These strategies primarily reduce urban temperatures through mechanisms such as shade provision, evapotranspiration, and surface albedo modification. Studies have shown that increasing urban greenery and strategically placing water bodies can effectively lower surface and air temperatures. However, most studies focus on either vegetation or water bodies in isolation, leaving a gap in understanding how the combined effects of these infrastructures could further alleviate UHI. To address this gap, many researchers have turned to computational fluid dynamics (CFD) simulations to model the interaction between land cover, water, and vegetation. These models can simulate the microclimate of urban environments, offering insights into how different configurations of green and blue spaces could mitigate urban heat. Despite this progress, few studies have integrated both field measurements and CFD simulations to validate the cooling effects of urban water and vegetation in a real-world context [5–7].

The cooling effect of vegetation on the urban thermal environment operates through four primary mechanisms: providing shade, facilitating evapotranspiration, altering surface albedo, and enhancing multi-sensory interactions [8,9]. Shade reduces surface temperatures by minimizing heat absorption and enhancing convective cooling [10]. For example, in summer, Speak et al. [11] found that tree shade could reduce the maximum pavement temperature by 292 K.

Another important mechanism is evapotranspiration, which cools the surrounding air by releasing water vapor [12]. In Würzburg, Germany, the evapotranspiration cooling of trees can reduce the air temperature by 3 K [13]. The surface albedo, or the reflectivity of a surface, also plays a significant role in cooling event [14]. Vegetated surfaces generally have a higher albedo than built-up surfaces, meaning they reflect more sunlight and absorb less heat. For example, the albedo of plants can reach 0.3, while that of typical urban surfaces such as concrete or asphalt is often between 0.1 and 0.2 [15]. Furthermore, green infrastructure can influence thermal perception through psychological factors, improving human comfort levels in urban environments [16]. Chen et al. [17] have quantitatively demonstrated that an increase in the greening ratio of urban spaces can significantly lower outdoor air temperatures. However, the relationship between greening and cooling is nonlinear: beyond a certain point, increasing greening no longer leads to proportional decreases in temperature, but rather reaches a maximum cooling effect.

Urban water bodies—including rivers, lakes, and ponds—offer significant cooling effects that help mitigate the UHI effect [18]. These effects occur through various processes, such as enhancing air circulation and heat absorption. Water bodies can significantly lower ambient temperatures and improve wind patterns, which is especially evident in areas near large bodies of water [19,20]. Smaller water bodies, such as ponds and lakes, can have a more localized impact, as their cooling effects are more prominent in the immediate surroundings.

Studies have shown that water bodies in cities can increase wind speed and lower temperatures in adjacent areas. Yang et al. [21] simulated the effect of a small lake on wind speed and temperature in the surrounding area of a city and found that the wind speed increased and the temperature decreased in areas with water. Similarly, Song et al. [22] analyzed the factors affecting the thermal and humid environment of the waterfront via the CFD method and found that the temperature of the area with a low-floor-area ratio and large ventilation corridor was more susceptible to the influence of water. Syafii et al. [23] evaluated the impact of various water configurations on the urban thermal environment,

with special emphasis on pedestrian comfort. The experimental results show that the thermal environment in urban canyons with ponds is better than that in urban canyons without ponds.

Additionally, water bodies' size and configuration play a key role in determining their cooling efficacy [24]. Xie et al. [25] discussed the cooling effect of water bodies on the urban environment in Wuhan, China, based on the measured data. The results showed that the main factor affecting the cooling effect of the urban water body system was the nature of the landscape, and the urban water body system with a relatively larger water body, more regular boundaries, and a simpler environment may be more effective in cooling the urban environment.

Numerical simulation plays a vital role in predicting the impacts of various urban planning measures on the thermal environment. CFD simulations are particularly useful for analyzing microclimates and the interaction between environmental parameters such as air temperature, wind speed, and humidity [26–28]. Early studies often relied on microclimate simulation tools to model mesoscale models, but due to computational limitations, many researchers have turned to CFD for micro-scale urban modeling [29].

CFD simulations provide valuable insights into the thermal dynamics of urban spaces, particularly when analyzing the impact of green and blue infrastructure on urban heat. For instance, studies by Tan et al. [30] and Bottillo et al. [31] examined how variations in surface temperature and thermal inertia influence urban airflow, using CFD models to simulate street canyons and building configurations. Robitu et al. [32] used standard CFD to simulate the impact of pools and trees on the surrounding thermal environment, and the results showed that trees and ponds should be regarded as improving the microclimate conditions of outdoor space.

In summer-hot and winter-cold regions, the urban heat island (UHI) effect significantly increases the cooling demand for buildings, with the UHI effect in certain areas of China leading to a 69.4% increase in building energy consumption [33]. To address this issue, research suggests that optimizing the layout of blue–green spaces is an effective solution. Zhou et al. [34] used remote sensing technology and geographic information systems (GISs) to analyze the role of blue–green spaces in Wuhan. The results showed that increasing green and water body coverage significantly lowers local temperatures, especially in dense urban areas. By optimizing the layout of these spaces, not only can the UHI effect be mitigated, but the city's climate adaptability and ecological health can also be improved. Additionally, Pan et al. [35] combined the urban canopy model (UCM) with the Weather Research and Forecasting (WRF) model to simulate the cooling effect of blue–green spaces. Their findings indicated that increasing water body or green coverage by 5–15% could effectively reduce both daytime and nighttime temperatures by approximately 0.71 °C. Therefore, optimizing the layout of blue–green spaces plays a crucial role in mitigating the urban heat island effect in summer-hot and winter-cold regions.

Based on the measured results of Wuhan's Dongxihu District, this paper studies the impact of water bodies and greening on the neighborhood microenvironment. By changing the proportion of water bodies and greening and changing the situation with or without water bodies and greening, it studies the changes in velocity speed and temperature in the neighborhood through comparison of various cases. In this paper, high-resolution 3D steady-state RANS CFD simulation is used. A comprehensive model of turbulence and radiation was used to determine the whole process, and the heat exchange between water and air was calculated. By comparing the influence of various cases on the thermal environment and wind environment, as well as the influence of their coupling on the neighborhood microenvironment, the design and layout of water and greening were guided.

2. Measurement and Analysis of the Site

2.1. Area Overview

The measurement was carried out on 4 June and 6 July 2024. The actual measurement site was the eastern campus area. The campus is located in Dongxihu District, Wuhan City. It is adjacent to Lingkonggang Avenue in the east, Gongxiang Road in the west, Wang'an Avenue in the north, and Binhe North Road in the south (Figure 1). Most of the buildings have 3 to 5 floors, and the spatial layout of the buildings is reasonable. There are various types of houses and complete facilities in the college, including architectural areas such as canteens, dormitories, libraries, and teaching buildings, as well as sports areas like playgrounds and gymnasiums (Figure 1). The campus has a total area of 480,000 m^2. The regional greening rate is over 30%, the building area occupies a relatively small proportion, and the ventilation is good.

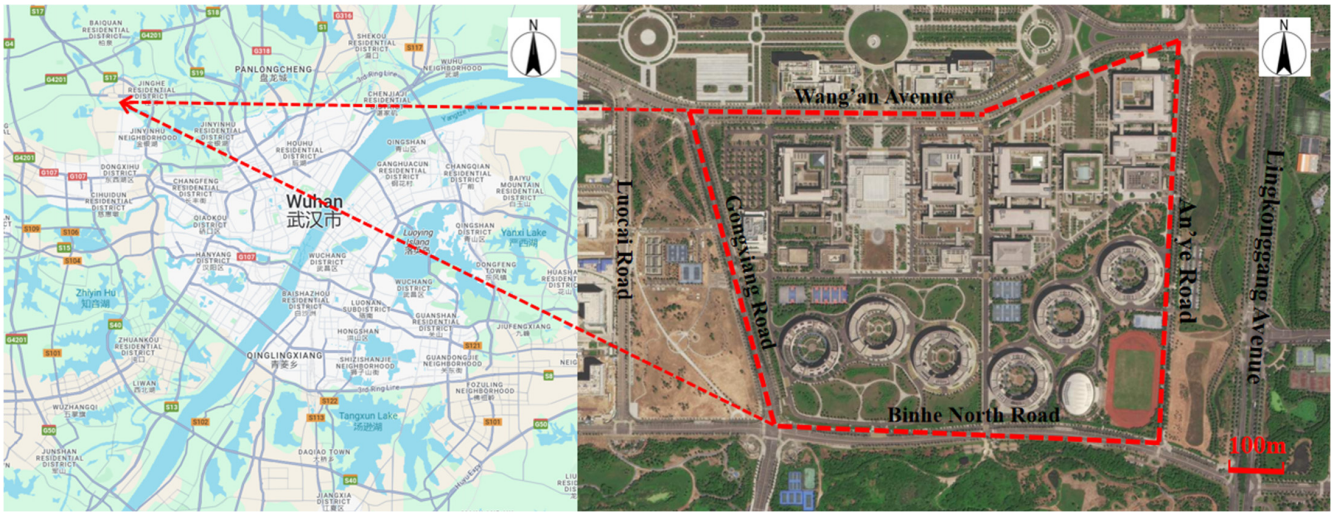

Figure 1. Location map and layout of the research area.

To understand the internal and surrounding environment of the campus, we measured the meteorological parameters along the campus and nearby roads. The instruments used for the measurements included the JT2023B anemometer, the JT2020 multifunctional tester, and the PC-8(A) mobile weather station (Figure 2). The specifications of the equipment are shown in Table 1. The measurements were taken at a height of approximately 1.5 m, which is typical for human breathing height. Due to limitations in the number of instruments and personnel, multiple observation points were selected on the campus and surrounding roads, with measurements conducted in phases. When selecting the measurement points, we considered factors such as greenery, road layout, and building density, and positioned the observation points at several representative locations accordingly.

Table 1. Table of equipment specifications.

Equipment	Place of Production	Manufacturer	Range of Measurement		Margin of Error	
			Temperature	Velocity	Temperature	Velocity
JT2023B	Beijing, China	Beijing Century Jiantong Technology Co., Ltd.	−20~70 °C	0–20 m/s	±0.5 °C	±(0.1 m/s ± 2% of the reading)
JT2020			−20~70 °C	0–2 m/s	±0.5 °C	±(0.05 m/s ± 2% of the reading)
				2–5 m/s		±(0.1 m/s ± 2% of the reading)
PC-8(A)	Liaoning, China	Jinzhou Sunshine weather technology Co., Ltd.	−40–120 °C	0~90 m/s	±0.1 °C	±0.1 m/s

Figure 2. The measuring instruments, from left to right, are the JT2023B wind speed tester, the JT2020 multifunctional tester, and the PC-8(A) mobile weather station.

2.2. Measurement Results and Analysis

2.2.1. Field Measurements of Campus and Surrounding Roads

The field measurements of campus and surrounding roads were conducted on the afternoon of 4 June 2024, during a cloudy day. The temperature ranged from 297.4 K to 298.6 K, with wind speeds recorded between 2 and 4 m/s (light breeze), and the wind came from the south and southeast. Given the measurement costs and accuracy considerations, the average temperature was recorded over 20 min intervals at each measuring point.

Initially, measurements were taken along three different roads surrounding the campus. For each road, two measurement points were selected and recorded. Following this, two rounds of measurements were conducted within the campus area. In each round, three different measurement points were selected, and as a result, six measurement points were used in total within the campus. The situation of each measuring point is shown in Figure 3.

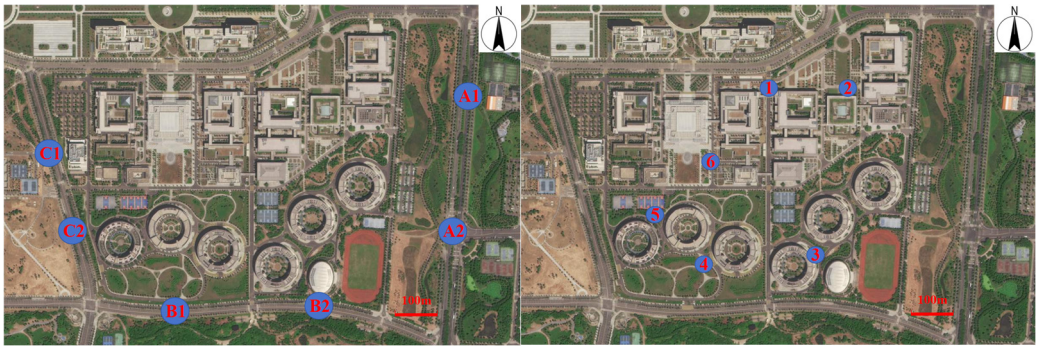

(**a**) Surroundings measurement (**b**) Internal measurement

Figure 3. Layout of measurement points.

The measured data are summarized in Tables 2 and 3. The temperature differences along the same road were consistently within 0.5 K, indicating a relatively uniform temperature distribution. The temperatures of the surrounding roads were all above 300.2 K, with the temperature near the left boundary being slightly lower than that at the right boundary, likely due to the proximity of the latter to the central campus area.

Table 2. The measured results of the surrounding roads.

Measuring Points	Airport Avenue (A Road)		North Binhe Road (B Road)		Shared Road (C Road)	
	10:25–10:45		11:40–12:00		12:40–13:00	
	Wind Speed (m/s)	Temperature (K)	Wind Speed (m/s)	Temperature (K)	Wind Speed (m/s)	Temperature (K)
1	1.168	301.6	1.761	302.2	1.355	300.3
2	1.545	302	1.047	302.1	1.160	300.5

Table 3. Campus interior measurement results.

Measuring Points	Time	Wind Speed (m/s)	Temperature (K)
1	15:50–16:10	2.02	299.5
2		1.06	299.3
3		3.68	299.5
4	16:45–17:05	1.08	299.1
5		2.39	299.3
6		0.94	299.3

Inside the campus, the heat island effect was not particularly pronounced due to good ventilation and moderate weather on that day. At measuring points 1 and 3, the temperatures were approximately 299.5 K, about 0.4 K higher than the surrounding temperature. The higher temperature at point 1 can be attributed to its location near the roadside, with less greenery and vehicle exhaust contributing to the temperature rise. At point 3, the heat island effect was more noticeable due to the relatively high building density in the area, which trapped heat around the measuring point.

The measurements show that the temperature difference between different areas was influenced by factors such as building density, greening, and proximity to main roads. As shown in Tables 1 and 2, areas closer to roads with fewer green spaces experienced higher temperatures, while areas surrounded by buildings with higher ventilation and more green infrastructure tended to maintain lower temperatures. These results underscore the importance of strategic planning in urban design to mitigate the UHI effect.

2.2.2. Field Measurements of Microclimates in Blue–Green Spaces Surrounding the Campus

The field measurements of microclimates in blue–green spaces surrounding the campus of measurements were carried out on 6 July 2024, under cloudy weather conditions in Dongxihu District, Wuhan. The temperature ranged from 308.2 K to 309.2 K, and the wind speed ranged from 2.5 m/s to 4.4 m/s (light to moderate breeze). The wind direction originated from the southwest. Given the measurement cost constraints, the average temperature at each measuring point was recorded over 30 min intervals, and the final measurement results were derived from the average value of these readings. Initially, measurements were taken on the main roads around campus, followed by four rounds of measurements inside and around the institute. The positions of all measuring points are shown in Figure 4, with the environmental wind speed and temperature data shown in Tables 4 and 5.

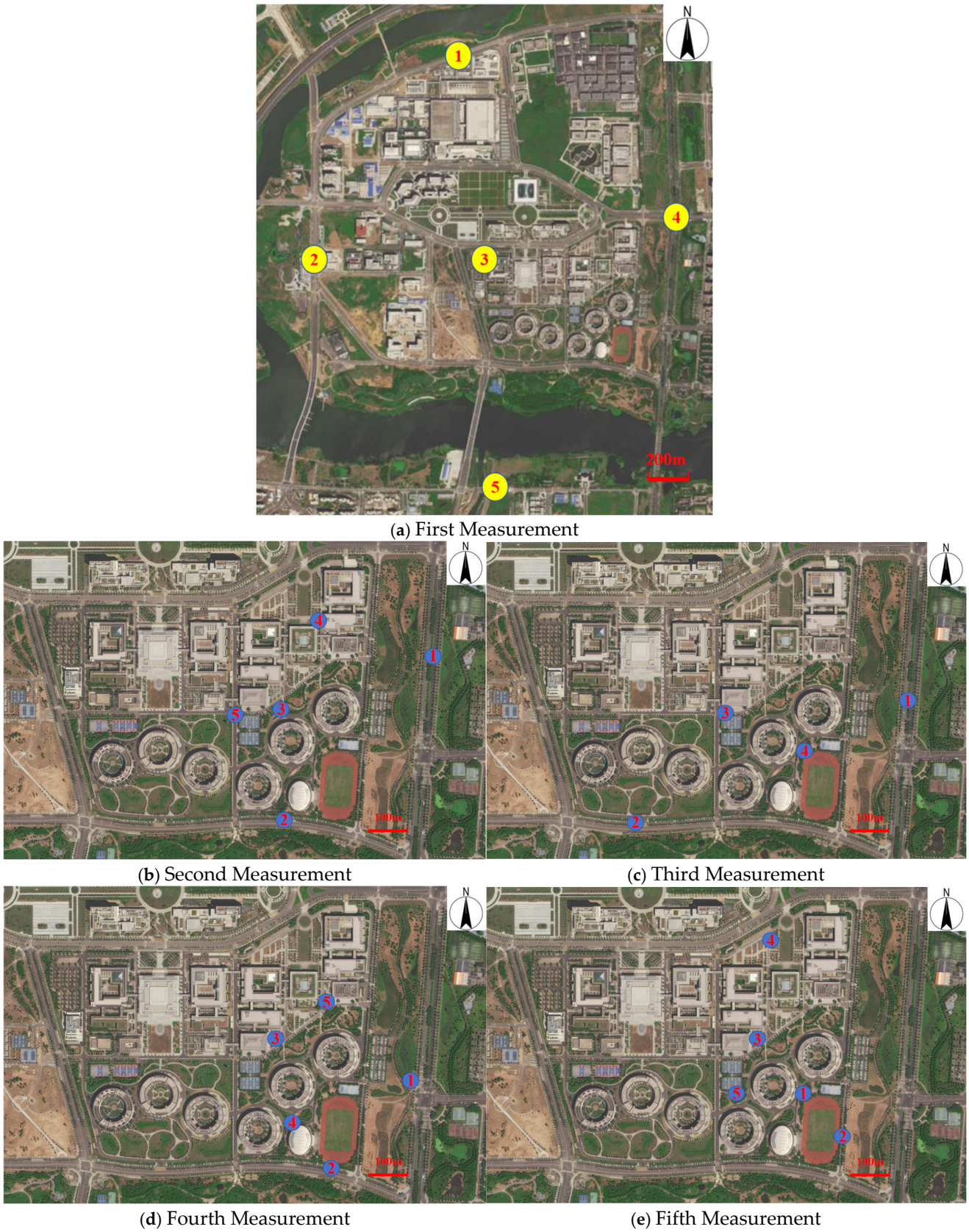

(**a**) First Measurement

(**b**) Second Measurement

(**c**) Third Measurement

(**d**) Fourth Measurement

(**e**) Fifth Measurement

Figure 4. The spatial arrangement of microclimate measurement points surrounding the campus.

Table 4. Temperature measurement results.

Measuring Point	Time	1	2	3	4	5
First	11:15–11:45	309.7 K	308.6 K	311.8 K	312.1 K	311.3 K
Second	14:45–15:15	310.5 K	309.7 K	311 K	310.9 K	310.6 K
Third	15:30–16:00	312.2 K	310.7 K	313 K	314.1 K	no
Fourth	16:25–17:55	309.7 K	310.3 K	310.9 K	308.7 K	311.4 K
Fifth	17:15–17:45	310.2 K	309.8 K	309.1 K	310.6 K	310.2 K

Table 5. Wind velocity measurement results.

Measuring Point	Time	2	3	4
First	11:15–11:45	7.01 m/s	3.25 m/s	3.62 m/s
Second	14:45–15:15	3.02 m/s	1.98 m/s	1.46 m/s
Third	15:30–16:00	2.63 m/s	1.75 m/s	1.07 m/s
Fourth	16:25–17:55	1.96 m/s	2.21 m/s	3.23 m/s
Fifth	17:15–17:45	1.34 m/s	1.11 m/s	0.88 m/s

The analysis of the first round of measurements showed a clear heat island effect in the central area, with temperature differences of 2–3 K compared to areas further from the center. This temperature increase was most prominent in the central area, where the UHI effect was most intense. In the second measurement, the temperatures at points 1 and 2 were lower than the intermediate temperature, and the heat island intensity reached up to 1.3 K. As for the third round of measurements, temperatures at points 3 and 4 in the central area were significantly higher than those at points 1 and 2, with the maximum heat island intensity reaching 1.8 K.

Interestingly, the fourth round of measurements showed a heat island intensity of 1.7 K, but at point 4, a lower temperature was observed due to higher wind speeds. The elevated wind speed at point 4 resulted in a cooler temperature, which was further amplified by the high density of greenery in the area. This phenomenon led to the formation of a localized low-temperature zone, which helped alleviate the heat island effect.

The fifth measurement revealed a decrease in the heat island intensity, which dropped to approximately 0.8 K. This reduction was likely due to the lower ambient temperature and reduced building energy consumption, which in turn reduced heat emissions from buildings. Notably, point 3 showed a temperature drop, even exhibiting a cold island effect. As seen in Figure 3, dense greenery, including trees, shrubs, and other plants, was located around point 3, which likely contributed to the formation of this cold island.

2.2.3. Comparative Analysis and Conclusions

By comparing the results from the five rounds of measurements, it is clear that the heat island effect was more intense over a larger area than within the confines of the campus. The data also showed that the heat island intensity varied depending on ambient temperature, with higher ambient temperatures leading to stronger heat island effects. This suggests that weather conditions play a crucial role in modulating building energy consumption, which subsequently affects the intensity of the heat island effect.

It is also evident that the intensity of the heat island effect is influenced by environmental factors, such as the surrounding greenery and building energy consumption. In areas with high levels of greenery, the heat island effect is alleviated, and even cold island phenomena can occur. Additionally, areas with higher wind speeds tend to have lower temperatures, further reducing the impact of the heat island effect.

3. Mathematical and Physical Models

3.1. Mathematical Model

The RNG k-ε model [36,37] was applied to simulate the temperature and wind speed conditions on the campus. This model offers reliable simulation results with an acceptable computational cost and is widely used in turbulence modeling. In Anasys fluent 2022R1, the time-average governing equation for the incompressible fluid continuity equation, momentum equation, and energy equation is as follows:

Continuity equation:

$$\frac{\partial u_i}{\partial t} = 0 \tag{1}$$

Momentum equation:

$$\frac{\partial u_i}{\partial t} + \rho\frac{\partial (u_i u_j)}{\partial x_j} = -\frac{\partial p}{\partial x_i} + \frac{\partial}{\partial x_j}\left\{(\mu + \mu_t)\left[\frac{\partial u_i}{\partial x_j} + \frac{\partial u_j}{\partial x_i}\right]\right\} + S_{u_i} \tag{2}$$

Here, u_i represents the vector velocity u (m/s), v (m/s), and w (m/s) in the x, y, and z directions; ρ is the air density, kg/m^3; p is the air pressure, pa; μ is the dynamic viscosity, pa·s; and S_u, S_v, and S_w are velocity source terms in the x, y, and z directions, respectively.

Turbulent kinetic energy k equation:

$$\rho\frac{\partial k}{\partial t} + \rho\frac{\partial k u_i}{\partial x_i} = \frac{\partial}{\partial x_j}\left[\alpha_k \mu_e \frac{\partial k}{\partial x_j}\right] + G_k + G_b - \rho\varepsilon - Y_M + S_k \tag{3}$$

Turbulent kinetic energy dissipation rate ε equation:

$$\rho\frac{\partial \varepsilon}{\partial t} + \rho\frac{\partial \varepsilon u_i}{\partial x_i} = \frac{\partial}{\partial x_j}\left[\alpha_\varepsilon \mu_e \frac{\partial \varepsilon}{\partial x_j}\right] + C_{1\varepsilon}\frac{\varepsilon}{k}(G_k + C_{3\varepsilon}G_b) - C_{2\varepsilon}\rho\frac{\varepsilon^2}{k} - R + S_\varepsilon \tag{4}$$

Here, k and ε represent the turbulent kinetic energy and the dissipation rate of turbulent kinetic energy, respectively; v is kinematic viscosity, m^2/s; $C_{1\varepsilon}$ = 1.42; $\mu_t = \rho C_\mu k^2/\varepsilon$; $C\mu$ = 0.0845; G_k represents the turbulent kinetic energy generation term due to the average velocity gradient; G_b is the turbulent kinetic energy generation term caused by welfare; Y_M represents the contribution of Liopogon expansion to the total dissipation rate in compressible turbulence; and S_k and S_ε are source terms, and the greening and water bodies in this model are calculated in the form of source terms.

Solar radiation has a great impact on the temperature of buildings and land. Therefore, the radiation heat transfer equation used in this simulation is as follows:

$$\frac{dI\left(\vec{r}, \vec{s}\right)}{ds} + (\alpha + \sigma_s)I\left(\vec{r}, \vec{s}\right) = \alpha n^2\frac{\sigma T^4}{\pi} + \frac{\sigma_s}{4\pi}\int I\left(\vec{r}, \vec{s}'\right)\phi\left(\vec{s}, \vec{s}'\right)d\Omega' \tag{5}$$

where $\vec{r}$ is the position vector, $\vec{s}$ is the direction vector, $\vec{s}'$ is the scattering direction vector, s refers to the path length, α is the absorption coefficient, n is the refractive index, σ_s is the scattering coefficient, σ is the Stefan–Boltzmann constant, 5.67×10^{-8} W/(m^{2}K^4), I is the radiation intensity, T is the local temperature, Φ is the phase function, and Ω' is the solid angle. The radiation intensity of this simulation is set at 400 W/m^2, the longitude of Dongxihu District is 114.13, the latitude is 30.67, and it belongs to the +8 time zone.

3.2. Physical Model

The simulation of this time is the campus in Dongxihu District, Wuhan, as shown in Figure 1 The model is designed to accurately simulate the real urban heat island, wind

environment, and pollutant distribution around the institute. The simulation domain of the campus area is 1250 m × 1200 m. According to the study of Franke et al. [38], since the tallest building in the block is 30 m, the simulated area of this model is 2450 m × 2050 m × 200 m. The three-dimensional physical model is shown in Figure 5b. To ensure the correctness of the verification results, the internal area of the campus is finely divided, as shown in Table 6.

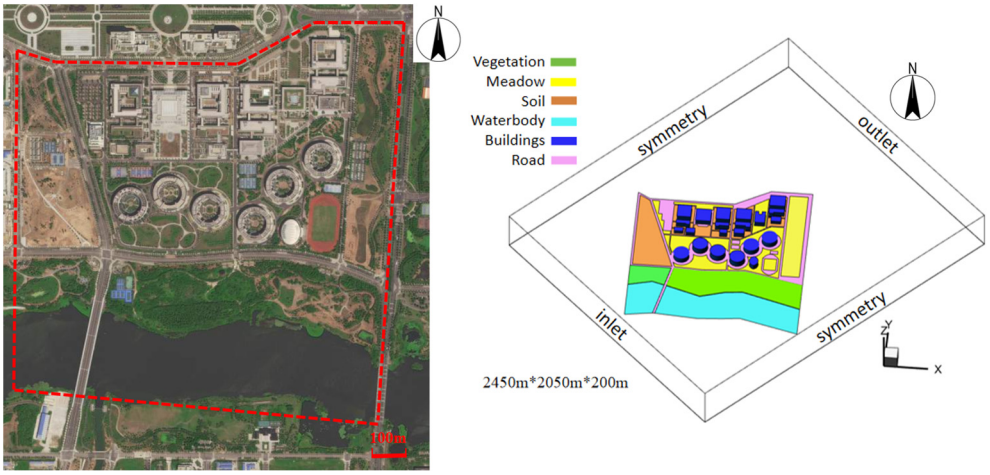

(**a**) (**b**)

Figure 5. Remote sensing satellite map (**a**) and numerical model (**b**) of simulated area.

Table 6. Proportion of underlying surface.

Underlying Surface Type	Ratio/%
water body	17.5
green belt	17.5
meadow	22.7
unit	10.7
soil	16.4
highroad	15.2

3.3. Boundary Conditions and Calculation Methods

3.3.1. Boundary Settings

For the simulation boundary conditions in this study, the inlet temperature is 308.7 K Additionally, the left, right, and upper boundaries were set as symmetry boundary conditions, and the outlet boundary was set as an outflow boundary, while the no-slip boundary condition was adopted at the walls and the ground. The inlet velocity boundary condition was modeled using the exponential law to represent the wind speed profile, as it is commonly used in environmental simulations [39,40]. Therefore, the exponential law was adopted in this paper to represent the wind speed profile. The velocity inlet was set to follow the widely adopted gradient wind model. At the outlet, the flow was assumed to be fully developed, and the outlet boundary condition was defined as "outflow". The side surfaces and the upper boundary were defined as symmetry boundary conditions.

The gradient wind formula is as follows:

$$u_{in} = u_{ref}\left(\frac{z}{z_{ref}}\right)^{0.16} \quad (6)$$

According to the calculations of Carlson et al. [41], the turbulent kinetic energy and its dissipation rate at the inlet are as follows:

$$k_{in} = 0.01 u_{ref}^2 \tag{7}$$

$$\varepsilon_{in} = C_\mu^{3/4} k_{in}^{3/2} / (kz) \tag{8}$$

where u_{ref} is the characteristic velocity at the reference height z_{ref}, which is 3.86 m/s; z_{ref} is set to 10 m; z represents the height above the ground, m; k is the von Kármán constant and is taken as 0.4; and the empirical constant C_μ = 0.09.

3.3.2. Water Body Evaporation and Heat Transfer Simulation

Since the simulation is conducted during daylight hours, a portion of the solar radiation absorbed by the water body is transferred to its depths, while another portion is utilized for the evaporation process. Since few scholars have conducted experiments on this, the calculation of the heat exchange between the water body and the air in this study is as follows [21]:

$$\varphi_n = \alpha \varphi_\varepsilon + \varphi_c \tag{9}$$

$$\varphi_\varepsilon = f(w_z)(e_w - e_\alpha) \tag{10}$$

$$\varphi_c = 0.47 f(w_z)(t_w - t_\alpha) \tag{11}$$

where ψ_e represents the heat absorption amount due to evaporation; ψ_c represents the convective heat exchange amount between the water body and the air; α is a conversion coefficient, and in this simulation, it is taken as 0.5; t_a and t_w are the air temperature and water surface temperature, respectively, K; e_w and e_a are the evaporation pressure of the air above the water surface and the air evaporation pressure, respectively, mmHg; and $f(w_z)$ = 9.2 + 0.46 $w_z{}^2$. The water body heat flow calculated in this study is -169.45 w/m^2.

3.3.3. Porous Media Simulation Setup for Vegetation

The plant canopy is composed of branches and leaves, with airflow channels formed between the leaves. Microscopically, leaves have the functions of depositing and purifying particulate matter. Macroscopically, the aerodynamic effects of the plant canopy impede air movement. Simulating the impact of the plant canopy on airflow at full scale is complex due to its sparse structure and the presence of pores. Consequently, the tree canopy can be modeled as a porous medium. The flow resistance of the airflow affected by the plant canopy is divided into viscous resistance and inertial resistance, which can be achieved by adding source terms to modify the corresponding equations [42]. The expressions are shown as follows:

$$S_{U_i} = -\rho C_d LAD U_i U \tag{12}$$

$$S_k = \rho C_d LAD(\beta_p U^3 - \beta_d U k) \tag{13}$$

$$S_\varepsilon = \rho C_d LAD \frac{\varepsilon}{k} \left(C_{\varepsilon 4} \beta_p U^3 - C_{\varepsilon 5} \beta_d U k \right) \tag{14}$$

where U_i represents the velocity component; S_U, S_k, and S_ε, respectively, stand for the source term of the continuity equation, the source term of the turbulent kinetic energy equation, and the source term of the turbulence dissipation rate equation; $S_U < 0$ indicates that plants have a weakening effect on airflow; and ρ denotes the air density. It should be noted that the plant leaf drag coefficient C_d is closely related to the vegetation type, and its typical value range is from 0.1 to 0.3. In this research paper, to effectively avoid the interference caused by different vegetation types, we uniformly set the value of C_d as the average value of 0.2. The plant leaf area density (LAD), which is defined as the ratio of

the leaf area to the volume of the plant canopy, usually has a value range from 0.5 m^{-1} to 2 m^{-1}, and in this study, it is selected as 2 m^{-1}. Based on the previous research results of Gromke and Blocken et al. [43], we further take β_p = 1, β_d = 5.1, and the empirical constants $C_{\varepsilon 4} = C_{\varepsilon 5}$ = 0.9. In this simulation, the height of vegetation on the left side of the vegetation area is 3 m, and that on the right side is 4 m.

3.3.4. Anthropogenic Heat Source Settings

Buildings act as significant heat sources in urban environments due to the heat released by air conditioning, heating systems, and various appliances. This effect is particularly pronounced during the summer months, contributing to the intensification of the urban heat island effect. The building heat index of each building is based on the building heat index calculated by Ma et al. [44]. The unified campus heat index of 118.54 kWh/(m^2a) is adopted.

3.3.5. Simulation Method

In this numerical simulation, the RNG k-ε turbulence model in ANSYS FLUENT 2022R1, a commercial computational fluid dynamics software based on the finite volume method, was adopted. For the convective terms, the second-order upwind difference scheme was used, while for the diffusion terms, the second-order upwind difference discrete scheme was employed. The SIMPLE algorithm was utilized for the coupling of pressure and velocity. When the residual values of variables such as flow velocities were less than 10^{-5} and the residual value of the energy equation was less than 10^{-6}, the calculation results were considered to have reached convergence.

3.4. Mesh Independence Verification

The tetrahedral grid is adopted for this model. To ensure the accuracy of the numerical simulation, it is necessary to verify the grid independence of the numerical grid. In this paper, the calculation results of three grid systems (with the numbers of grids being 7,197,800, 5,825,900, and 4,219,200, respectively) under the same calculation conditions and the same setup working conditions are compared. As shown in Figure 6, the maximum calculation errors of the temperature and velocity distributions along the Z direction in the (500,500) position for the three grid systems under the same conditions are all less than 5%. When the number of grids is 4,219,200, the error of the calculation result is the largest. However, when the number of grids is 5,825,900 and 7,197,800, there is no obvious deviation in the calculation results. It can be concluded that further increasing the number of grids will not cause significant changes to the calculation results. Therefore, the grid system with 5,825,900 grids can ensure the accuracy of the calculation results.

The simulated grid is a hexahedral mesh, with a maximum grid size of 40 m in the study area. To ensure calculation accuracy, the internal region is refined, with the building and ground areas having a grid size ranging from 5 to 8 m, while the green plant areas are refined with a grid size of 4 m. The total grid count is 5,825,900, with a resolution exceeding 0.5 m.

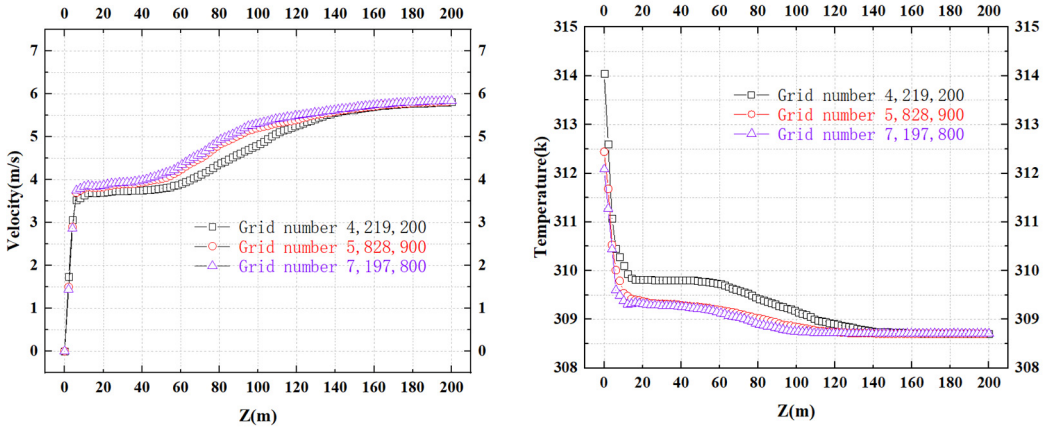

(**a**) Velocity Verification (**b**) Temperature Verification

Figure 6. Grid independence verification.

3.5. Model Validation

To validate the simulation results, actual measurement data from 4 June 2024 were used. The test site, located at the campus in Dongxihu District, Wuhan, was chosen for its representative urban environment. The measurements were conducted under cloudy conditions, with the temperature ranging from 297.4 K to 298.6 K, wind speeds between 2 and 4 m/s (gentle breeze, levels 2–3), and winds from the south and southeast. These conditions were selected to reflect typical summer weather patterns in the region.

In order to ensure data accuracy and minimize measurement costs, the average temperature at each measuring point was recorded over a period of 20 min. The environmental conditions in Dongxihu District from 2:00 pm to 5:00 pm on that day were used as the basis for the simulation. The simulation results were then compared with the actual measured data.

A total of six internal measurement points were established, as shown in Figure 7, with each measuring point located at a height of 1.5 m. These points were carefully distributed within the area to capture spatial variations in temperature and wind speed.

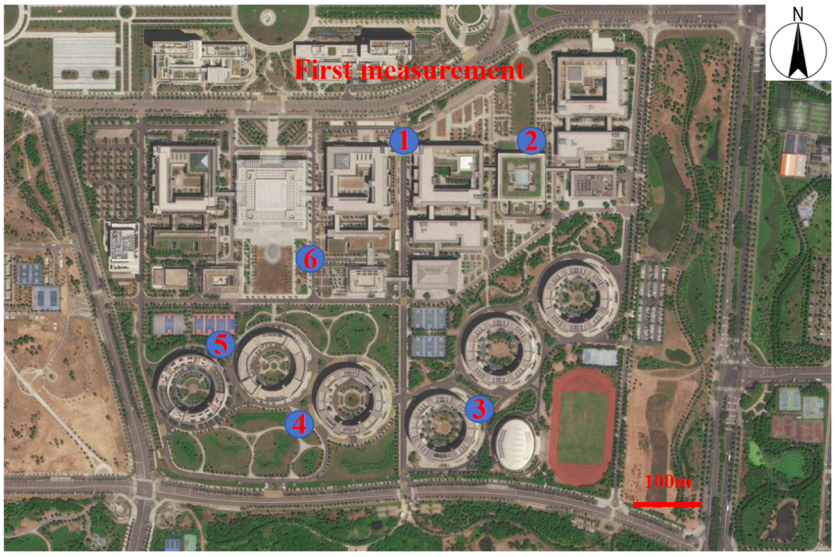

Figure 7. The layout of measuring points inside the campus.

Table 7 shows the results, where it can be seen that the simulated wind speeds closely match the measured values. The maximum error between the simulation and the actual measurements is 21.7%, which is within an acceptable range for this type of simulation.

This suggests that the model can reasonably replicate the wind behavior in the study area under typical summer conditions.

Table 7. Comparison between the measured and simulated wind speeds.

Measuring Point	Simulated Wind Speed (m/s)	Measured Wind Speed (m/s)	Relative Error
1	2.33	2.02	15.3%
2	0.83	1.06	21.7%
3	3.79	3.68	3.0%
4	1.16	1.08	7.4%
5	2.65	2.39	10.9%
6	1.05	0.94	11.7%

This validation process not only confirms the reliability of the simulation results but also demonstrates the model's ability to accurately simulate urban environmental conditions in Dongxihu District. The good agreement between the simulated and measured data supports the use of this model for future studies on urban heat islands and environmental planning in similar urban areas.

4. Results and Discussion

4.1. Simulation Case Settings

In this simulation, four cases (shown in Table 8) of the campus were first analyzed to compare the wind speed and temperature distributions of each case. To better analyze the impacts of greenery and water bodies on the thermal and wind environments of the block, the simulation area was partitioned as illustrated in Figure 8. By examining each case and each partition, the influences of greenery and water bodies on the thermal and wind environments of the block were investigated, which could offer certain guiding significance for subsequent urban planning.

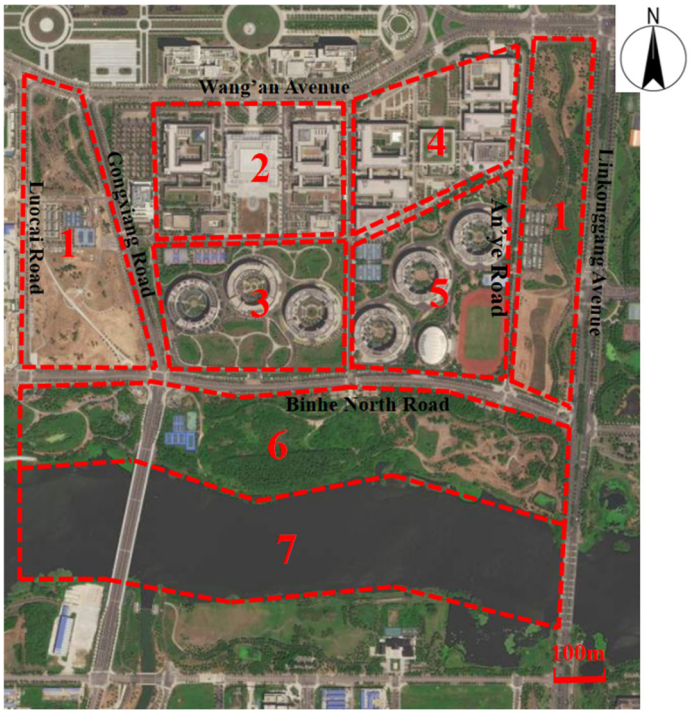

Figure 8. Regional division of research area.

Table 8. Case setting.

Case	Vegetation	Water Body
Case 1	no	no
Case 2	no	yes
Case 3	yes	no
Case 4	yes	yes

4.2. Wind Velocity Distribution

According to Figures 9 and 10, the average wind speeds of case 1 and case 2 show a nearly overlapping phenomenon, suggesting that the water body has a negligible impact on the wind speed in the block. By comparing case 1 and case 3, it can be seen that the presence of greenery has a substantial influence on the wind speed at a height of 1.5 m within the block. As shown in Figure 10, due to the effect of green plants like trees and bushes in the green belt, the wind speed at this position decreases by approximately 2 m/s. The existence of the green belt leads to a reduction in wind speed of about 0.5 m/s in the area close to it while having little effect on the wind speed in the regions far from the green belt. This is because the vegetation such as trees in the green belt blocks the upstream wind, directly affecting the wind speed near the ground surface in the vicinity of the green belt. For the regions at a relatively long distance, the impact is minor due to the full development of the flow.

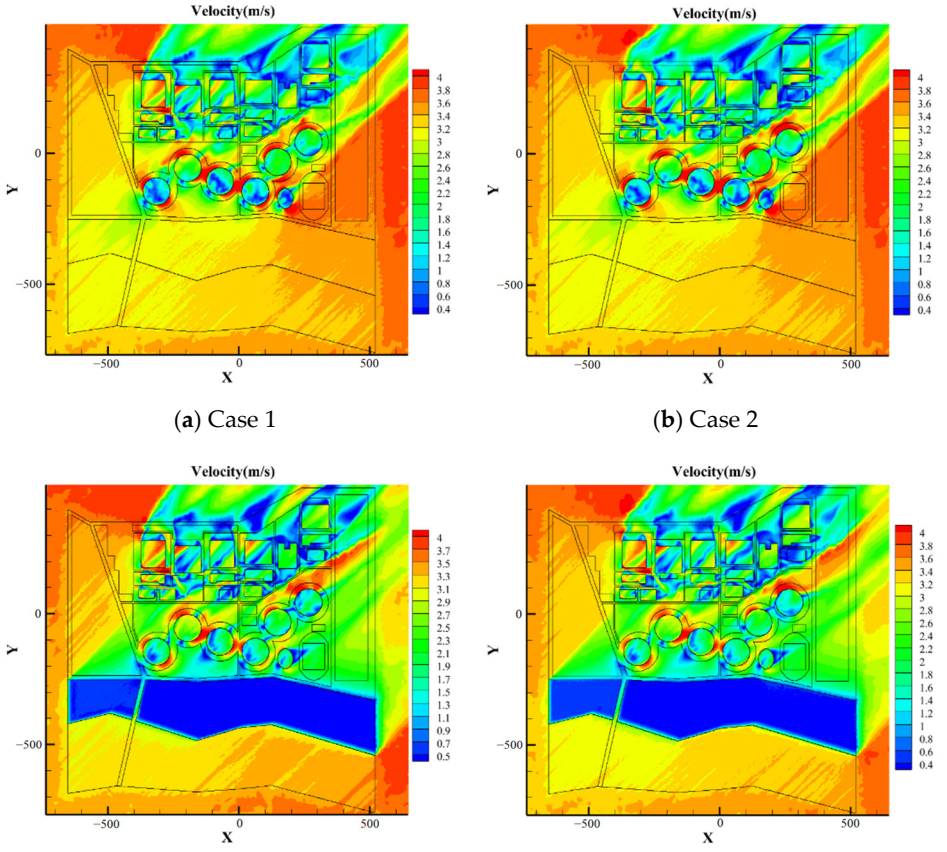

(**a**) Case 1 (**b**) Case 2

(**c**) Case 3 (**d**) Case 3

Figure 9. Contours of wind velocity at Z = 1.5 m.

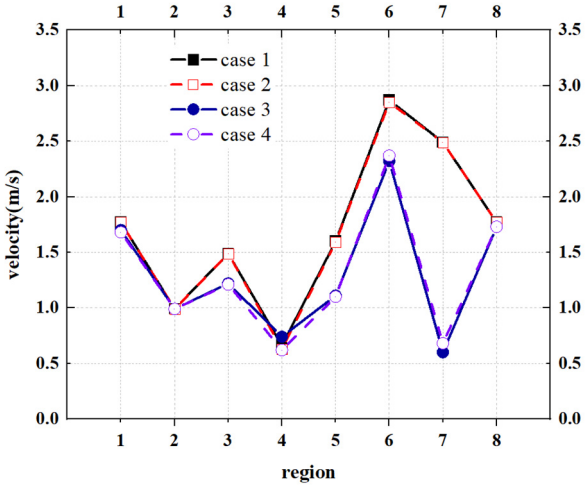

Figure 10. Average wind speed in the research area.

In Figure 10, the wind speeds in region 3 and region 5 are lower than the average wind speeds in region 4 and region 6. A comparison of the contours also shows significant differences in the maximum wind speed ranges between these regions. Owing to the differences in building forms as well as the impacts of building density and layout, it is observable that the wind speed around circular buildings has noticeably increased, which is caused by the abnormal wind speed due to the generation of vortex streets. In contrast, such abnormal phenomena scarcely occur around square buildings, and the wind speed distribution shows a high wind speed on the windward side and a low wind speed on the leeward side. Another reason is that the building layout in the square building area is compact, while that in the cylindrical building area is relatively dispersed. Moreover, under the influence of vegetation, the average wind speed in region 3 decreased by 0.3 m/s, while the wind speed in region 5 decreased by 0.5 m/s. This is because the vegetation height on the left side of the vegetation area is lower than that on the right side, so increasing the greening height will further reduce the wind speed in the downstream area.

Figure 11 shows the distribution map of turbulent kinetic energy at a height of 1.5 m. It is observed that the effect of water bodies does not have an impact on the turbulent kinetic energy in the downstream area, while vegetation has a greater impact on the downstream area. The closer the distance to the vegetation, the more obvious the change in turbulent kinetic energy, and the farther the area, the weaker the effect. Based on the distribution of turbulent kinetic energy inside the campus in the figure, it is found that under the influence of greenery, the turbulent kinetic energy inside the college in the downstream area increases. This is because the vegetation plays a role in disturbing the upstream wind, resulting in an increase in vortices in the downstream area and an increase in turbulent kinetic energy. According to Figure 9, it is found that in some downstream areas, due to the obstruction of vegetation, the wind speed does not decrease significantly. This is because the eddy current here increases, resulting in an abnormal increase in the wind speed at the beginning of region 4. In addition, the turbulent kinetic energy around the circular building is higher than that around the square building, which is due to the phenomenon of the Karman vortex street, which causes the wind speed around the circular building to increase. Therefore, the disturbance effect of the circular building on the surrounding wind is significantly higher than that of the square building, making the wind speed around the circular building higher than that of the square building. In comparison to observing the phenomenon of abnormal increase in flow velocity in the middle area of Anye Road in Figure 8 for case 1 and case 3, it can be seen from Figure 9 that the turbulent kinetic energy

here is significantly enhanced, and due to the strong eddy current generated here, the wind speed here is enhanced.

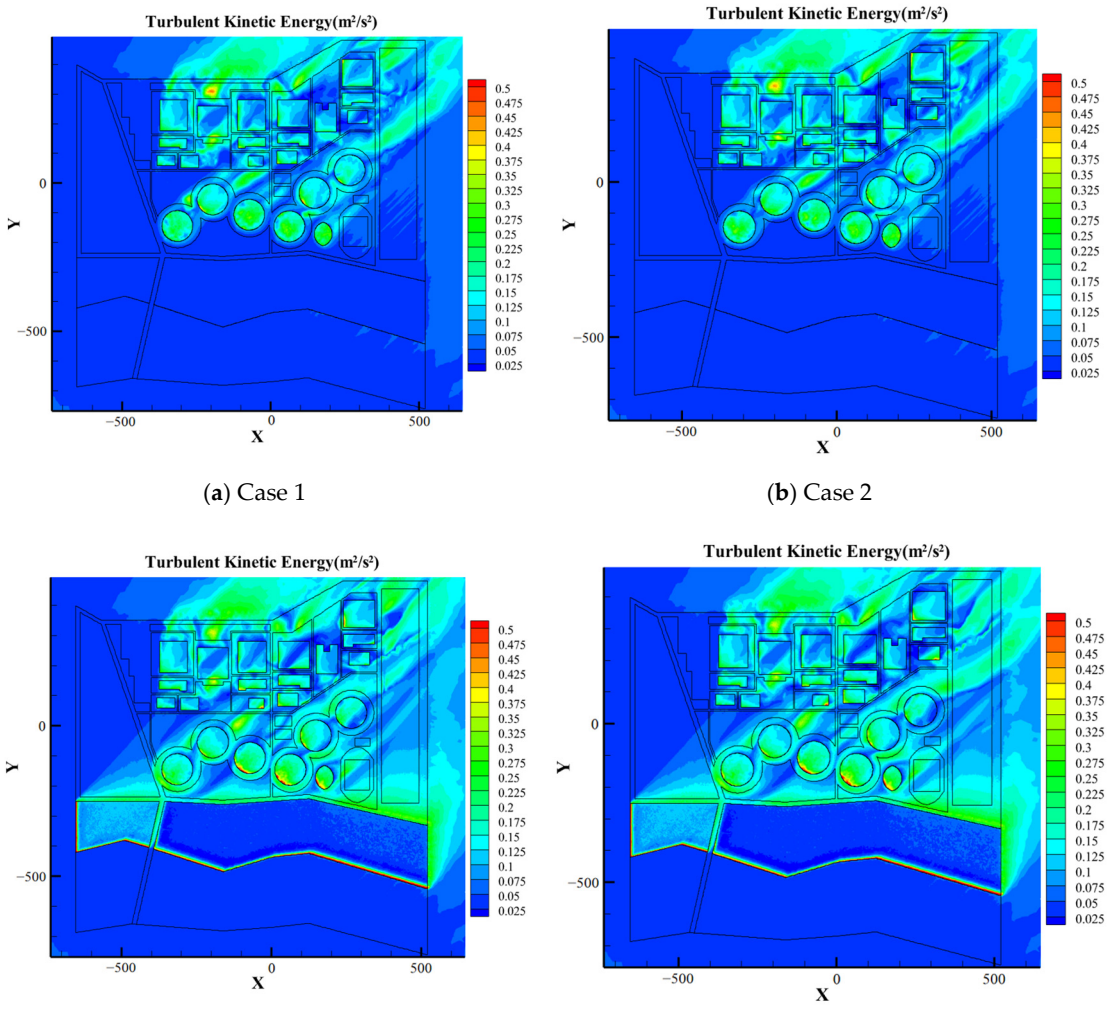

(**a**) Case 1 (**b**) Case 2

(**c**) Case 3 (**d**) Case 4

Figure 11. Distribution of turbulent kinetic energy at Z = 1.5 m.

4.3. Temperature Distribution

Figure 12 illustrates the average temperature distribution across different regions under cases 1 to 4. From Figure 11, it can be observed that in case 1, the temperature in areas around the buildings remains consistently high, approximately 319 K. However, in case 2, the presence of the water body results in a significant cooling effect, particularly in regions downstream of the water body. The cooling effect intensifies with proximity to the water body and leads to a temperature reduction of approximately 2 °C to 6 °C in the downstream regions. Similarly, case 3 demonstrates the cooling effect of greenery. As seen in Figure 13, the vegetation areas cause a significant temperature drop in the adjacent regions, with the cooling effect diminishing with increasing distance from the greenery. However, some areas within the greenery exhibit higher temperatures, which may be attributed to low wind speeds that reduce the dissipation of heat and lead to localized warming. Case 4, which combines the effects of both water bodies and greenery, shows a cooling effect in the downstream regions. However, this combined cooling effect is not linear, and the synergy between greenery and water bodies does not produce significantly greater cooling than when each element is considered separately. This is likely due to the distinct mechanisms of cooling: the water body dissipates solar heat through evaporation and heat transfer to

deeper layers, while the greenery interacts with the wind flow, redistributing heat and altering temperature patterns.

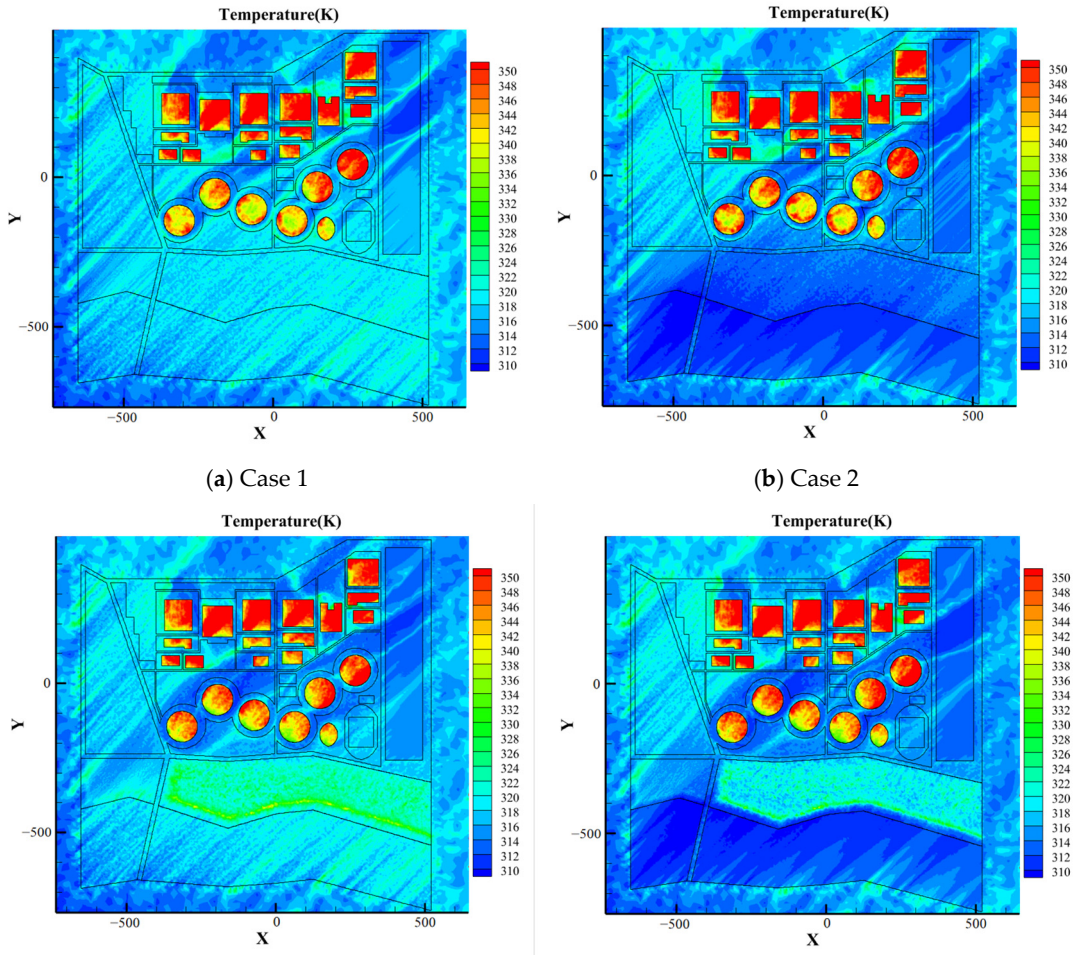

(**a**) Case 1 (**b**) Case 2

(**c**) Case 3 (**d**) Case 4

Figure 12. Contours of temperature at Z = 1.5 m.

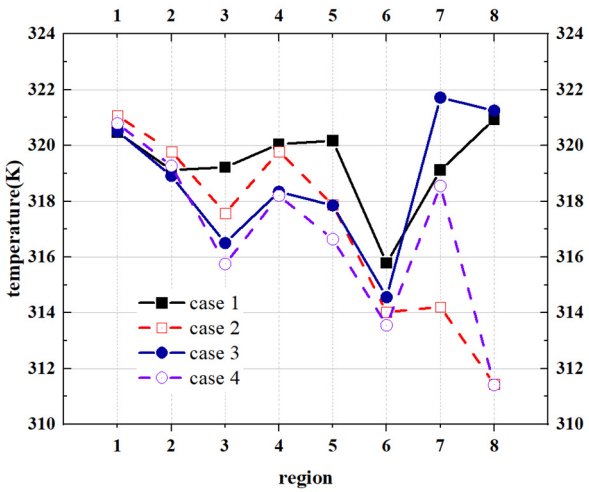

Figure 13. Average temperature in the research area.

From Figure 13, it is evident that regions 1 and 2, which are not directly downstream of the water body or greenery, experience minimal temperature changes across all cases. In contrast, regions 3, 4, 5, and 6, located directly downstream, show substantial temperature

reductions under cases 2, 3, and 4. Notably, the cooling effect of greenery surpasses that of the water body in these regions due to the water body's limited influence at greater distances. Furthermore, in areas where both greenery and water bodies coexist, the temperature distribution shows an interesting pattern: the water body maintains a consistently lower surface temperature, while the vegetation shows slight localized warming due to direct solar radiation heating the leaves at a height of 1.5 m. This distinction highlights the complementary but independent cooling mechanisms of water bodies and greenery.

In summary, analyses of Figures 12 and 13 reveal that both water bodies and greenery play crucial roles in reducing temperatures within the block. While water bodies are effective in lowering temperatures through evaporation and heat absorption, greenery interacts dynamically with wind and solar radiation, resulting in more localized temperature variations. The combination of these elements provides cooling effects but does not amplify the temperature reduction significantly beyond their individual contributions.

By comparing the distribution of wind speed and temperature, it is evident that both greenery and water bodies significantly improve the thermal comfort of downstream areas. However, since greenery tends to reduce wind speed in the downstream region, blocks with water bodies are generally more comfortable than those with greenery during hot summer conditions. When both greenery and water bodies are combined, the cooling effect is not significantly enhanced compared to the effect of a single water body or greenery alone.

5. Conclusions and Prospects

This study combines field measurements and CFD simulations to investigate the effects of blue–green infrastructure on microclimatic heat islands within a campus area. The findings demonstrate that both vegetation and water bodies provide significant cooling effects, reducing temperatures by 0–6 K in downstream areas, with impacts more pronounced near the blue–green spaces. The research underscores the nonlinear relationship between the thermal environment and the combination of water bodies and vegetation, highlighting the importance of their spatial arrangement for optimal performance.

Field measurements revealed clear patterns of temperature variation, with heat island effects near roads and cold island phenomena in densely vegetated areas. While greenery and water bodies both contribute to cooling, the mechanisms differ: vegetation reduces temperatures but decreases wind speed, which can affect thermal comfort, while water bodies tend to maintain wind flow and provide consistent cooling. These differences suggest that the placement of water bodies upstream and vegetation downstream can maximize their combined effects in summer.

Despite these valuable insights, this study has limitations that warrant further exploration. The field measurements were conducted in stages and covered a limited spatial extent due to constraints in resources and equipment. Additionally, CFD modeling simplifies urban layouts, which may introduce discrepancies between simulated and actual results. Most importantly, the research focuses exclusively on summer conditions, where heat island effects are most pronounced, leaving the impacts of blue–green infrastructure during other seasons unexamined.

The role of blue–green infrastructure is not confined to mitigating summer heat. In regions with distinct seasons, these systems can also stabilize temperatures in winter. Water bodies may release stored heat during cold periods, acting as thermal buffers, while vegetation can provide wind shelter and reduce heat loss. Such effects could help address cold island phenomena in winter and further enhance urban thermal comfort. Expanding the scope of this research to include year-round measurements and simulations will provide a more comprehensive understanding of the dual roles of blue–green spaces in mitigating both heat and cold islands.

In conclusion, blue–green infrastructure offers a powerful strategy for addressing urban heat islands and improving microclimatic conditions. By carefully designing the spatial arrangement of water bodies and vegetation, urban planners can optimize these cooling effects and enhance thermal comfort in diverse urban environments. Future research should focus on refining these strategies for different climatic conditions and exploring their seasonal dynamics, ensuring that blue–green systems contribute to sustainable urban development throughout the year.

Author Contributions: Conceptualization, T.M. and Y.H.; methodology, T.S. and Y.C.; software, B.L.; validation, T.S. and S.H.; formal analysis, Y.H. and S.H.; investigation, Y.L.; resources, T.M.; data curation, B.L. and D.Y.; writing—original draft preparation, T.S. and Y.H.; writing—review and editing, C.P. and T.M.; visualization, Y.C.; supervision, T.M.; project administration, Y.C.; funding acquisition, T.M. All authors have read and agreed to the published version of the manuscript.

Funding: This research was supported by the National Natural Science Foundation of China (Grant No. 52278123), the CITIC General Institute of Architectural Design and Research (No. 2022ZXKYD30100), and the Scientific Research Foundation of the Wuhan University of Technology (Grant Nos. 40120237 and 40120551).

Institutional Review Board Statement: Not applicable.

Informed Consent Statement: Not applicable.

Data Availability Statement: The data presented in this study are available through email upon request to the corresponding author. The data are not publicly available due to privacy.

Acknowledgments: The author would like to acknowledge the support of all those who contributed to the completion of this work.

Conflicts of Interest: Author Yanhua Chen was employed by the company CITIC General Institute of Architectural Design and Research Co., Ltd. The remaining authors declare that the research was conducted in the absence of any commercial or financial relationships that could be construed as a potential conflict of interest.

References

1. Stabler, L.B.; Martin, C.A.; Brazel, A.J. Microclimates in a Desert City Were Related to Land Use and Vegetation Index. *Urban For. Urban Green.* **2005**, *3*, 137–147. [CrossRef]
2. Karimi, A.; Sanaieian, H.; Farhadi, H.; Norouzian-Maleki, S. Evaluation of the Thermal Indices and Thermal Comfort Improvement by Different Vegetation Species and Materials in a Medium-Sized Urban Park. *Energy Rep.* **2020**, *6*, 1670–1684. [CrossRef]
3. Gachkar, D.; Taghvaei, S.H.; Norouzian-Maleki, S. Outdoor Thermal Comfort Enhancement Using Various Vegetation Species and Materials (Case Study: Delgosha Garden, Iran). *Sustain. Cities Soc.* **2021**, *75*, 103309. [CrossRef]
4. Bavarsad, F.S.; Di Giuseppe, E.; D'Orazio, M. Numerical Assessment of the Impact of Roof Albedo and Thermal Resistance on Urban Overheating: A Case Study in Southern Italy. In *Sustainability in Energy and Buildings 2021*; Springer: Singapore, 2022; pp. 125–134, ISBN 978-981-16-6269-0.
5. Saneinejad, S.; Moonen, P.; Carmeliet, J. Comparative Assessment of Various Heat Island Mitigation Measures. *Build. Environ.* **2014**, *73*, 162–170. [CrossRef]
6. Lin, B.; Li, X.; Zhu, Y.; Qin, Y. Numerical Simulation Studies of the Different Vegetation Patterns' Effects on Outdoor Pedestrian Thermal Comfort. *J. Wind Eng. Ind. Aerodyn.* **2008**, *96*, 1707–1718. [CrossRef]
7. Chen, H.; Ooka, R.; Huang, H.; Tsuchiya, T. Study on Mitigation Measures for Outdoor Thermal Environment on Present Urban Blocks in Tokyo Using Coupled Simulation. *Build. Environ.* **2009**, *44*, 2290–2299. [CrossRef]
8. Lenzholzer, S.; De Vries, S. Exploring Outdoor Thermal Perception—A Revised Model. *Int. J. Biometeorol.* **2020**, *64*, 293–300. [CrossRef] [PubMed]
9. Gunawardena, K.R.; Wells, M.J.; Kershaw, T. Utilising Green and Bluespace to Mitigate Urban Heat Island Intensity. *Sci. Total Environ.* **2017**, *584–585*, 1040–1055. [CrossRef] [PubMed]
10. Yu, Q.; Ji, W.; Pu, R.; Landry, S.; Acheampong, M.; O' Neil-Dunne, J.; Ren, Z.; Tanim, S.H. A Preliminary Exploration of the Cooling Effect of Tree Shade in Urban Landscapes. *Int. J. Appl. Earth Obs. Geoinf.* **2020**, *92*, 102161. [CrossRef]

11. Speak, A.; Montagnani, L.; Wellstein, C.; Zerbe, S. The Influence of Tree Traits on Urban Ground Surface Shade Cooling. *Landsc. Urban Plan.* **2020**, *197*, 103748. [CrossRef]
12. Winbourne, J.B.; Jones, T.S.; Garvey, S.M.; Harrison, J.L.; Wang, L.; Li, D.; Templer, P.H.; Hutyra, L.R. Tree Transpiration and Urban Temperatures: Current Understanding, Implications, and Future Research Directions. *BioScience* **2020**, *70*, 576–588. [CrossRef]
13. Rahman, M.A.; Hartmann, C.; Moser-Reischl, A.; Von Strachwitz, M.F.; Paeth, H.; Pretzsch, H.; Pauleit, S.; Rötzer, T. Tree Cooling Effects and Human Thermal Comfort under Contrasting Species and Sites. *Agric. For. Meteorol.* **2020**, *287*, 107947. [CrossRef]
14. Rizwan, A.M.; Dennis, L.Y.C.; Liu, C. A Review on the Generation, Determination and Mitigation of Urban Heat Island. *J. Environ. Sci.* **2008**, *20*, 120–128. [CrossRef] [PubMed]
15. Tan, C.L.; Wong, N.H.; Tan, P.Y.; Jusuf, S.K.; Chiam, Z.Q. Impact of Plant Evapotranspiration Rate and Shrub Albedo on Temperature Reduction in the Tropical Outdoor Environment. *Build. Environ.* **2015**, *94*, 206–217. [CrossRef]
16. Knez, I.; Thorsson, S.; Eliasson, I.; Lindberg, F. Psychological Mechanisms in Outdoor Place and Weather Assessment: Towards a Conceptual Model. *Int. J. Biometeorol.* **2009**, *53*, 101–111. [CrossRef] [PubMed]
17. Chen, C.; Yue, Y.; Jiang, W. Numerical Simulation on Cooling Effects of Greening for Alleviating Urban Heat Island Effect in North China. *AMM* **2014**, *675–677*, 1227–1233. [CrossRef]
18. Cao, B.; Chen, Q.; Du, M.; Cheng, Q.; Li, Y.; Liu, R. Simulation Analysis of the Cooling Effect of Urban Water Bodies on the Local Thermal Environment. *Water* **2022**, *14*, 3091. [CrossRef]
19. Lap, B.Q.; Tuan, N.V.; Hamagami, K.; Iguchi, S.; Mori, K.; Hirai, Y. Formation and Disappearance of Thermal Stratification in a Small Shallow Lake. *J. Fac. Agric. Kyushu Univ.* **2009**, *54*, 251–259. [CrossRef]
20. Cheng, Y.; Liu, X.; Zeng, Z.; Liu, S.; Wang, Z.; Tang, X.; He, B.-J. Impacts of Water Bodies on Microclimates and Outdoor Thermal Comfort: Implications for Sustainable Rural Revitalization. *Front. Environ. Sci.* **2022**, *10*, 940482. [CrossRef]
21. Yang, L.; Liu, X.; Qian, F. Research on Water Thermal Effect on Surrounding Environment in Summer. *Energy Build.* **2020**, *207*, 109613. [CrossRef]
22. Song, X.; Liu, J.; Zhao, Y. Effect of Design Factors on the Thermal Environment in the Waterfront Area. *Procedia Eng.* **2017**, *205*, 2677–2682. [CrossRef]
23. Syafii, N.I.; Ichinose, M.; Kumakura, E.; Jusuf, S.K.; Chigusa, K.; Wong, N.H. Thermal Environment Assessment around Bodies of Water in Urban Canyons: A Scale Model Study. *Sust. Cities Soc.* **2017**, *34*, 79–89. [CrossRef]
24. Li, G.; Pan, Y.; Yang, L. Numerical Simulation of the Effects of Water Surface in Building Environment. In Proceedings of the 3rd International Conference On Energy Equipment Science And Engineering (ICEESE 2017), Beijing, China, 28–31 December 2017; IoP Publishing Ltd.: Bristol, UK, 2018; Volume 128, p. 012072.
25. Xie, Q.; Ren, L.; Yang, C. Regulation of Water Bodies to Urban Thermal Environment: Evidence from Wuhan, China. *Front. Ecol. Evol.* **2023**, *11*, 983567. [CrossRef]
26. Yushkov, V.P.; Kurbatova, M.M.; Varentsov, M.I.; Lezina, E.A.; Kurbatov, G.A.; Miller, E.A.; Repina, I.A.; Artamonov, A.Y.; Kallistratova, M.A. Modeling an Urban Heat Island during Extreme Frost in Moscow in January 2017. *Izv. Atmos. Ocean. Phys.* **2019**, *55*, 389–406. [CrossRef]
27. Otte, T.L.; Lacser, A.; Dupont, S.; Ching, J.K.S. Implementation of an Urban Canopy Parameterization in a Mesoscale Meteorological Model. *J. Appl. Meteorol.* **2004**, *43*, 1648–1665. [CrossRef]
28. Gao, Z.; Hou, Y.; Chen, W. Enhanced Sensitivity of the Urban Heat Island Effect to Summer Temperatures Induced by Urban Expansion. *Environ. Res. Lett.* **2019**, *14*, 094005. [CrossRef]
29. Liu, Q.; Dong, Q.; Zhang, L.; Sun, C. Summer Cooling Island Effects of Blue-Green Spaces in Severe Cold Regions: A Case Study of Harbin, China. *Build. Environ.* **2024**, *257*, 111539. [CrossRef]
30. Tan, Z.; Dong, J.; Xiao, Y.; Tu, J. A Numerical Study of Diurnally Varying Surface Temperature on Flow Patterns and Pollutant Dispersion in Street Canyons. *Atmos. Environ.* **2015**, *104*, 217–227. [CrossRef]
31. Bottillo, S.; De Lieto Vollaro, A.; Galli, G.; Vallati, A. Fluid Dynamic and Heat Transfer Parameters in an Urban Canyon. *Sol. Energy* **2014**, *99*, 1–10. [CrossRef]
32. Robitu, M.; Musy, M.; Inard, C.; Groleau, D. Modeling the Influence of Vegetation and Water Pond on Urban Microclimate. *Sol. Energy* **2006**, *80*, 435–447. [CrossRef]
33. Wang, S.; Wang, Z.; Zhang, Y.; Fan, Y. Characteristics of Urban Heat Island in China and Its Influences on Building Energy Consumption. *Appl. Sci.* **2022**, *12*, 7678. [CrossRef]
34. Zhou, W.; Yu, W.; Zhang, Z.; Cao, W.; Wu, T. How Can Urban Green Spaces Be Planned to Mitigate Urban Heat Island Effect under Different Climatic Backgrounds? A Threshold-Based Perspective. *Sci. Total Environ.* **2023**, *890*, 164422. [CrossRef]
35. Pan, Z.; Xie, Z.; Wu, L.; Pan, Y.; Ding, N.; Liang, Q.; Qin, F. Simulation of Cooling Island Effect in Blue-Green Space Based on Multi-Scale Coupling Model. *Remote Sens.* **2023**, *15*, 2093. [CrossRef]
36. Shih, T.-H.; Liou, W.W.; Shabbir, A.; Yang, Z.; Zhu, J. A New k-ϵ Eddy Viscosity Model for High Reynolds Number Turbulent Flows. *Comput. Fluids* **1995**, *24*, 227–238. [CrossRef]

37. Yakhot, V.; Orszag, S.A.; Thangam, S.; Gatski, T.B.; Speziale, C.G. Development of Turbulence Models for Shear Flows by a Double Expansion Technique. *Phys. Fluids A* **1992**, *4*, 1510–1520. [CrossRef]
38. Franke, J.; Baklanov, A. *Best Practice Guideline for the CFD Simulation of Flows in the Urban Environment: COST Action 732 Quality Assurance and Improvement of Microscale Meteorological Models*; Meteorological Inst: Toronto, ON, Canada, 2007.
39. Rajapaksha, I.; Nagai, H.; Okumiya, M. A Ventilated Courtyard as a Passive Cooling Strategy in the Warm Humid Tropics. *Renew. Energy* **2003**, *28*, 1755–1778. [CrossRef]
40. Leung, K.K.; Liu, C.-H.; Wong, C.C.C.; Lo, J.C.Y.; Ng, G.C.T. On the Study of Ventilation and Pollutant Removal over Idealized Two-Dimensional Urban Street Canyons. *Build. Simul.* **2012**, *5*, 359–369. [CrossRef]
41. Carlson, T.N.; Dodd, J.K.; Benjamin, S.G.; Cooper, J.N. Satellite Estimation of the Surface Energy Balance, Moisture Availability and Thermal Inertia. *J. Appl. Meteor.* **1981**, *20*, 67–87. [CrossRef]
42. Katul, G.G.; Mahrt, L.; Poggi, D.; Sanz, C. ONE-and TWO-Equation Models for Canopy Turbulence. *Bound.-Layer Meteorol.* **2004**, *113*, 81–109. [CrossRef]
43. Gromke, C.; Blocken, B. Influence of Avenue-Trees on Air Quality at the Urban Neighborhood Scale. Part II: Traffic Pollutant Concentrations at Pedestrian Level. *Environ. Pollut.* **2015**, *196*, 176–184. [CrossRef] [PubMed]
44. Ma, H.; Du, N.; Yu, S.; Lu, W.; Zhang, Z.; Deng, N.; Li, C. Analysis of Typical Public Building Energy Consumption in Northern China. *Energy Build.* **2017**, *136*, 139–150. [CrossRef]